nature communications

Article

https://doi.org/10.1038/s41467-026-68740-6

Interfacial water regulation on Ru single atoms doped Co_3O_4 toward efficient electrochemical hydrogenation of quinoxaline

Received: 8 September 2025

Accepted: 15 January 2026

Linghu Meng[1], Tian-yi Dai[2], Jilong Li[1], Chengjin Dong[1], Fengyan Wang[1], Ming Peng[1], Qing Jiang[2], Tong-hui Wang[2] & Yongwen Tan[1]

Electrochemical hydrogenation of quinoxaline presents a promising alternative to traditional methods, yet is suffering from low current density and Faradaic efficiency due to the hampered hydrogenation process. Herein, we develop a cocatalytic system of Ru single atoms doped Co_3O_4 nanosheet (Ru_{SA}/ns-Co_3O_4) to optimize the interfacial H_2O behavior by tuning the Ru single atoms concentration for accelerating the electrochemical hydrogenation of quinoxaline, which enables remarkable Faradaic efficiency of 82% toward 1,2,3,4-tetrahydroquinoxaline at high current density of 200 mA cm^{-2}. Detailed experimental and theoretical studies reveal that Ru single atoms trigger interfacial charge redistribution, inducing an asymmetric local electric field that reconstructs interfacial H_2O molecules into an H-down configuration. This reorientation remodels the hydrogen-bonded water network, shortens the distance between hydrogen atoms and the Co_3O_4 surface, regulates $K{\bullet}H_2O$ availability, and enhances H_2O dissociation to supply H*. Consequently, the membrane electrode assembly electrolyser exhibits a long-term stability of >100 h at 200 mA cm^{-2}. Our findings highlight the prospect of interfacial water microenvironment for electrochemical hydrogenation of unsaturated N-heterocyclic compounds, with promising applications for the electrosynthesis of other valuable chemicals.

The hydrogenation of unsaturated N-heterocyclic compounds holds significant importance in liquid organic hydrogen carrier (LOHC) technology and pharmaceutical synthesis, attracting extensive research interest due to its application potential[1–3]. For example, quinoxaline hydrogenation to 1,2,3,4-tetrahydroquinoxaline as one of the most common hydrogen storage reactions, which is dependent on thermochemcial hydrogenation using H_2 or organic hydrogen donor as the source of protons and electrons under high temperature and pressure conditions[4,5], resulting in significant energy waste and by-product (Fig. 1a). In contrast, renewable energy-powered electrochemical hydrogenation (ECH) using water as the green hydrogen source provides an efficient and sustainable approach to achieve hydrogenation of unsaturated compounds under ambient conditions[6–8]. Unfortunately, the sluggish water dissociation and poor proton supply rate cause the insufficient kinetics of the hydrogenation process, the current quinoxaline to 1,2,3,4-tetrahydroquinoxaline

---

[1]College of Materials Science and Engineering, State Key Laboratory of Advanced Design and Manufacturing Technology for Vehicle Body, Hunan University, Changsha, China. [2]Key Laboratory of Automobile Materials (Jilin University), Ministry of Education, and School of Materials Science and Engineering, Jilin University, Changchun, China. e-mail: twang@jlu.edu.cn; tanyw@hnu.edu.cn

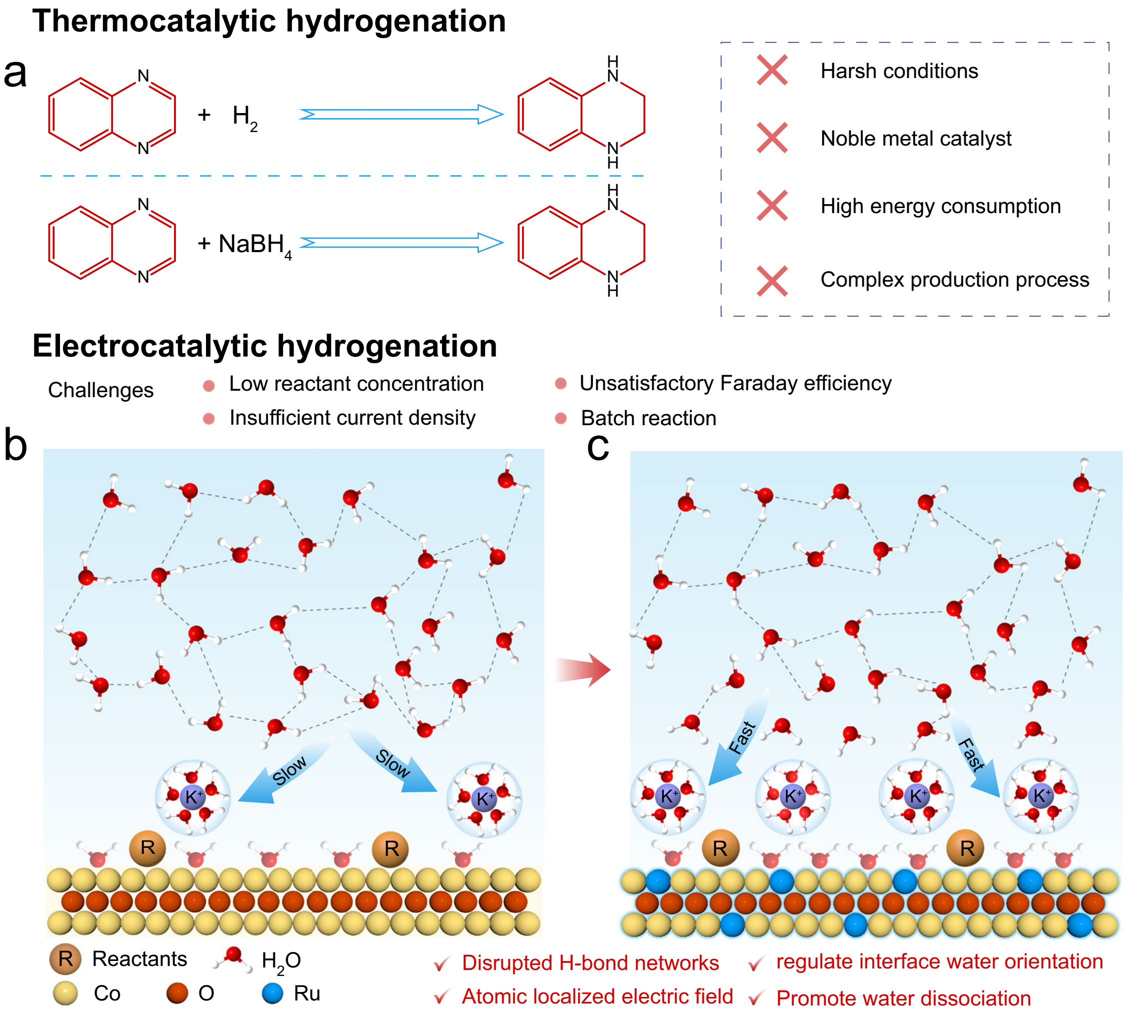

Fig. 1 | Schematic comparisons of 1,2,3,4-tetrahydroquinoxaline production pathways. a Conventional industrial thermocatalytic route. **b** Traditional water dissociation for electrochemical process. **c** The proposed single atoms regulating the water orientation for the electrochemical process. The single-atom doping strategy involves water orientation in H-down mode and facilitates the formation of more K•H_2O for water dissociation.

conversion via the ECH process suffers from the unsatisfactory current densities (<50 mA cm^{-2}) and Faradaic efficiency, as well as poor stability[9–12], thus resulting in industrial-incompatible production rates.

To achieve high efficiency and selectivity in ECH, adequate proton supply is the prerequisite for guaranteeing the electrochemical hydrogenation steps of substrates[13–15]. However, the production of protons is required to overcome the high thermodynamic energy barrier of H_2O dissociation[16–18], inhibiting the hydrogenation efficiency and selectivity in alkaline environments (Fig. 1b). Actually, interfacial H_2O not only dissociate into adsorbed active hydrogen (H*) on the electrode surface to provide the hydrogen source but also form an hydrogen-bond (HB) networks to affect proton transfer[19,20]. In view of this, the unique characteristics of interfacial H_2O structure can greatly determine the thermodynamics and kinetics of active hydrogen generation, which can be readily influenced by the local microenvironment[21–23]. Currently, most of the previous reports focus on the surface modification/electrolyte additives to modulate active hydrogen (H*) behavior for enhancing the proton supply[24–26]. However, excessive addition of additives could reduce the conductivity of the electrolyte and hinder proton transport[27–29]. In comparison, regulating the interactions between the catalyst surface and interfacial H_2O via local electric fields to reorient H_2O molecules and reconstruct H-bond networks represents an excellent strategy for controlling water dissociation activity (Fig. 1c)[30,31]. However, those methods cannot precisely regulate the structure of H-bond networks, and its correlation with ECH performance remains unclear. Therefore, it is highly important to modulate the local microenvironment of H_2O molecules on the electrocatalyst surface to meet the H* demands of ECH reactions by regulating the dissociation activity of interfacial H_2O, which has been rarely explored.

Here, we construct a series of Ru single-atom doped Co_3O_4 nanosheet electrocatalysts (denoted as Ru_{SA}/ns-Co_3O_4) to precisely regulate the availability of K•H_2O for accelerating the hydrogenation process of quinoxaline at an industrial-level current density. By integrating theoretical simulations and calculations, and in situ spectra characterizations, revealing the Ru_{SA}/ns-Co_3O_4 cocatalytic system generates an asymmetric localized electric field on the catalytic surface, which could induce interfacial H_2O molecules into an H-down reconfiguration, facilitating stepwise H_2O activation and efficient H* generation for boosting the hydrogenation of quinoxaline. As the proof-of-concept electrocatalyst, the Ru_{SA}/ns-Co_3O_4-0.7% with the optimal K•H_2O ratio enables efficient ECH of quinoxaline to a 1,2,3,4-tetrahydroquinoxaline with selectivity of ~100% and Faradaic efficiency of 82% at 200 mA cm^{-2}, surpassing recently reported state-of-the-art electrocatalysts. This enables membrane electrode assembly (MEA) stable operation for 100 h at a current density of 200 mA cm^{-2}. Importantly, the Ru_{SA}/ns-Co_3O_4 catalyst also shows excellent universality for electrochemical hydrogenation of various unsaturated N-heterocyclic compounds.

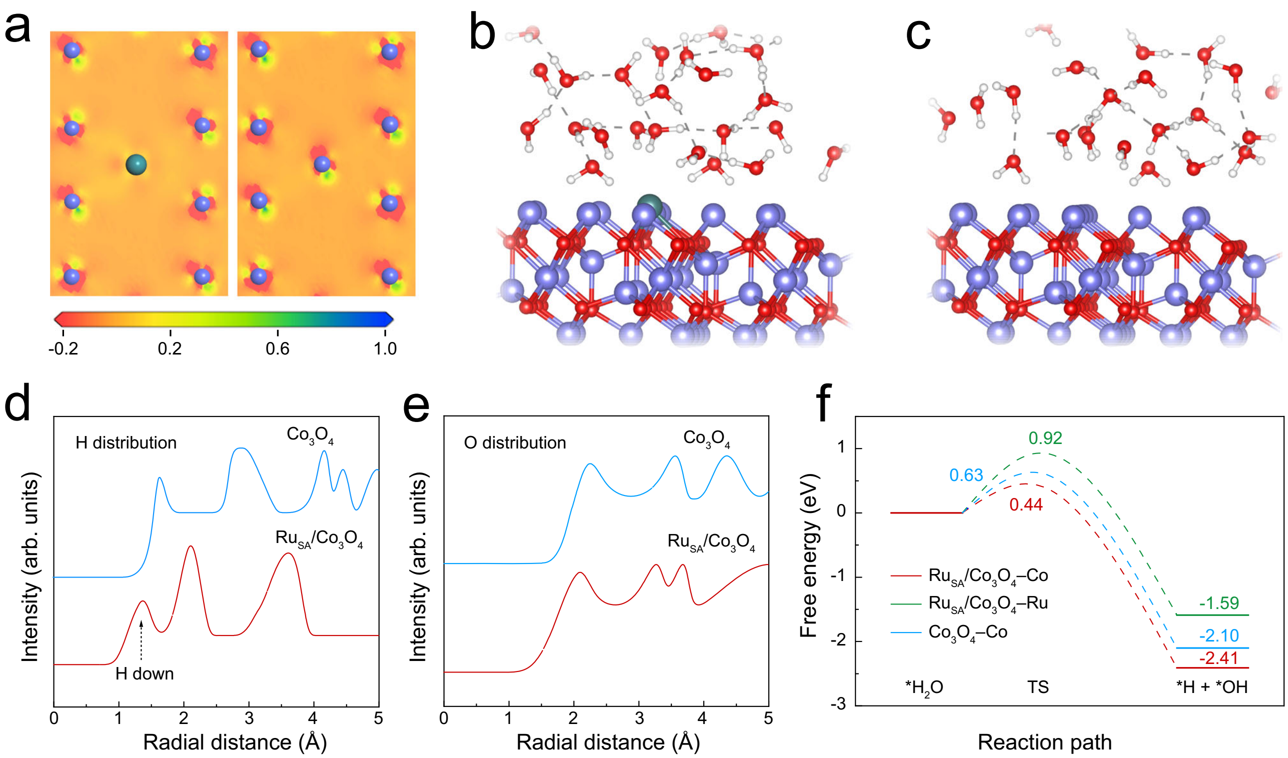

Fig. 2 | DFT calculations. a Charge density analyses of Ru_{SA}/Co_3O_4 and Co_3O_4. Interfacial H_2O orientation simulated by AIMD simulations of **b** Ru_{SA}/Co_3O_4, **c** Co_3O_4. **d, e** The statistical H and O distribution distance in the z-direction of the adsorbed H_2O molecules at the interface. **f** DFT calculation for the energy barriers of H_2O dissociation process on the Ru_{SA}/Co_3O_4 and Co_3O_4. Blue: Co atoms, Red: O atoms, White: H atoms; green: Pd atoms. Source data are provided as a Source Data File.

These results indicate the great potential of the electrochemical hydrogenation of unsaturated N-heterocyclic compounds as a next-generation sustainable hydrogen storage technology[32].

Results

Theoretical investigations

Density functional theory (DFT) calculations were first performed to analyse the redistribution of charge density, indicating that the introduction of Ru single atoms leads to a strong and asymmetric atomic localized electric field (Fig. 2a). Ab initio molecular dynamics (AIMD) simulations were further conducted to explore atomic structures of interfacial H_2O on Ru_{SA}/Co_3O_4 and Co_3O_4 surfaces (Fig. 2b, c). The local electric field around the Ru SAs affects the configuration of H_2O molecules and the distributions of H and O at the interface. The average distance between H and the surface of Co atoms is significantly reduced from 1.60 Å to 1.38 Å (Fig. 2d), while the distance between O and catalyst surface is not changed significantly in these two cases (Fig. 2e). This evidence further indicates that asymmetric atomic localized electric fields facilitate the regulation of interfacial water orientation and enable precise manipulation of the reaction microenvironment. We further employed DFT calculations to investigate the energy barrier for H_2O dissociation on the Co_3O_4 and Ru_{SA}/Co_3O_4 (Fig. 2f, Supplementary Figs. 1–3). The results show that the energy barrier of H_2O dissociation on the Co atoms of Ru_{SA}/Co_3O_4 is 0.44 eV, which is much lower than that Co atoms of Co_3O_4 (0.63 eV) and Ru atoms of Ru_{SA}/Co_3O_4 (0.91 eV). These findings indicate that the interfacial H_2O reorientation induced by local electric field at the active site can optimize the H_2O dissociation process, significantly reducing the kinetic barrier for forming H*.

Synthesis and characterizations of Ru_{SA}/ns-Co_3O_4

Inspired by the concept, such Ru single atoms doped Co_3O_4 nanosheets were prepared through a facile chemcial dealloying and annealing process (Supplementary Fig. 4). Typtically, the precursor $Ru_{0.2}Co_{19.8}Al_{80}$ alloy ribbons were prepared by single-roller melt spinning. Then the metallic Al of these precursor alloys was completely dealloyed in a KOH solution to obtain Ru doped CoO_x nanosheets (Supplementary Figs. 5 and 6). Finally, uniform Ru-doped Co_3O_4 nanosheets were obtained after annealing at 300 °C under Ar atmosphere, demonstrating that the introduction of Ru did not alter the morphology of the Co_3O_4 nanosheets (Fig. 3a, Supplementary Fig. 7). The X-ray diffraction (XRD) patterns show typical spinel structure with *Fd-3m* space groups for ns-Co_3O_4 and Ru_{SA}/ns-Co_3O_4 (Supplementary Fig. 8a)[33]. Owing to the introduction of the Ru atoms, the diffraction peaks of Ru/ns-Co_3O_4 slightly shifted to a higher angle than that of ns-Co_3O_4, suggesting the atomic-level Ru was well incorporated into the Co_3O_4 crystal lattice and causes the local structure contraction (Supplementary Fig. 8b)[34]. Aberration–corrected high–angle annular dark–field scanning transmission microscopy (HAADF–STEM) image of Ru_{SA}/ns-Co_3O_4 reveals clear lattice fringes with a spacing of 1.82 Å, which can assigned to the interplanar spacing of the (331) plane of Co_3O_4 (Fig. 3b). Isolated dots with particularly high intensity were clearly observed, which are assigned to Ru atoms because of the higher atomic number of Ru (Supplementary Fig. 9). These results reveal that Ru atoms are doped into the lattice structure of Co_3O_4. Furthermore, the energy-dispersive spectroscopy (EDS) mapping images indicate a homogenous distribution of atomic Ru species in the Co_3O_4 nanosheets (Supplementary Fig. 10). Subsequent composition evaluation of Ru_{SA}/ns-Co_3O_4 by inductively coupled plasma optical emission spectrometry (ICP-OES) confirms that Ru has an atomic ratio of 0.7% (Supplementary Table 1). X-ray absorption spectroscopy (XAS) was conducted with the aim of distinguishing the electronic structure and the local atomic environment of Ru_{SA}/ns-Co_3O_4. The normalized Ru K-edge X-ray absorption near-edge structure (XANES) spectrum is positioned between those of Ru foil and RuO_2 (Fig. 3c), indicating the distinctive electronic structure of $Ru^{\delta+}$ ($0 < \delta < 4$), as confirmed by the X-ray photoelectron spectroscopy (XPS) results of Ru 3*p* in the Ru_{SA}/

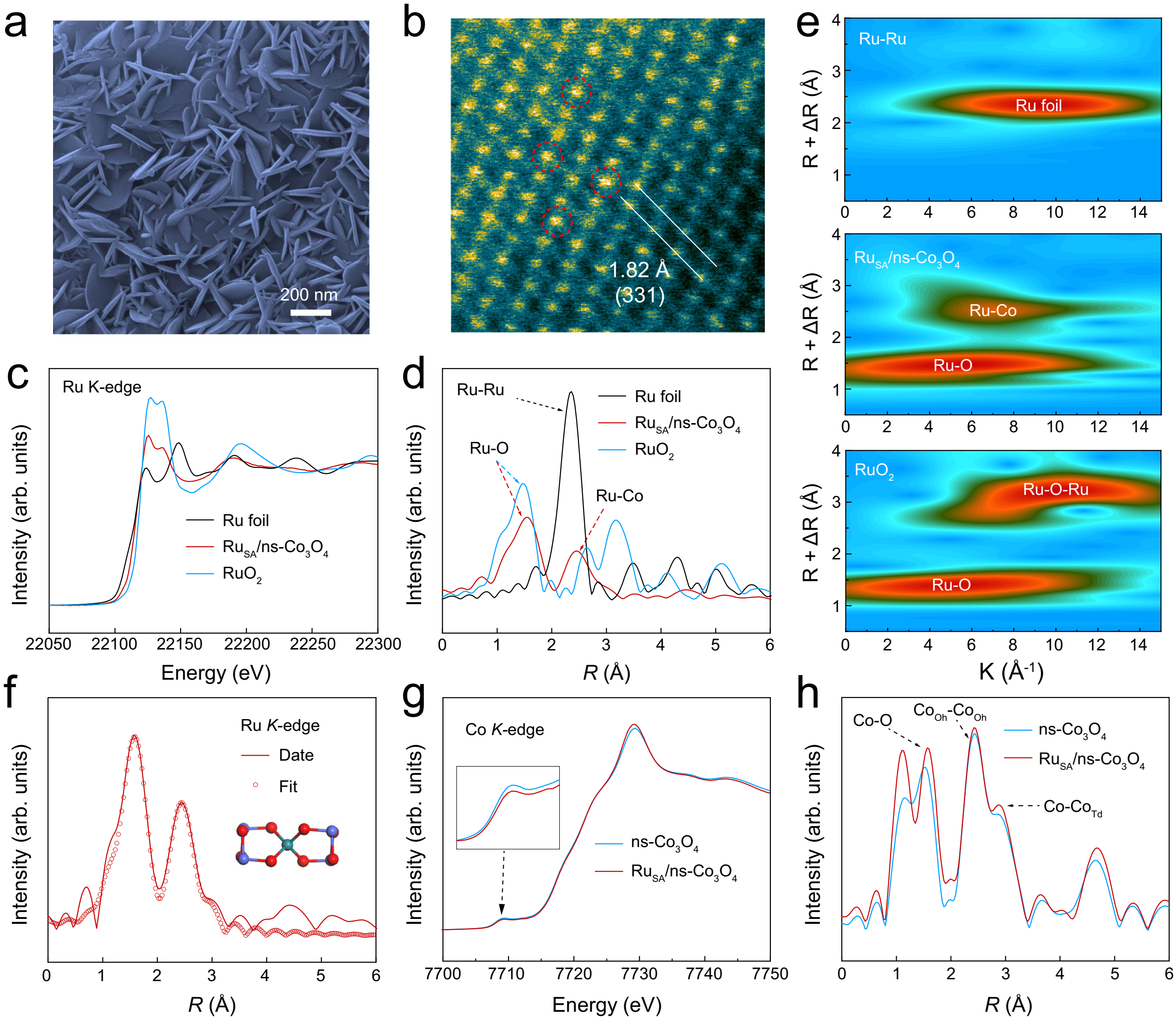

Fig. 3 | Structural characterizations of $Ru_{SA}/ns-Co_3O_4$. **a** SEM image of $Ru_{SA}/ns-Co_3O_4$. **b** HAADF-STEM image of $Ru_{SA}/ns-Co_3O_4$. **c** Ru K-edge XANES of Ru foil, RuO_2, and $Ru_{SA}/ns-Co_3O_4$. **d** Fourier transformed magnitudes of Ru K-edge EXAFS spectra for Ru foil, RuO_2, and $Ru_{SA}/ns-Co_3O_4$. **e** WT-EXAFS Ru K-edge spectra of Ru foil, $Ru_{SA}/ns-Co_3O_4$ and RuO_2. **f** k^2-weighted Fourier transformed EXAFS at the Ru K-edge of the $Ru_{SA}/ns-Co_3O_4$ with EXAFS fitting. **g** Co K-edge XANES of $ns-Co_3O_4$ and $Ru_{SA}/ns-Co_3O_4$. **h** Fourier transformed magnitudes of Co K-edge EXAFS spectra for $ns-Co_3O_4$ and $Ru_{SA}/ns-Co_3O_4$. Source data are provided as a Source Data File.

$ns-Co_3O_4$ (Supplementary Fig. 11). The Fourier transform (FT) of the Ru K-edge extended X-ray absorption fine structure (EXAFS) spectra of $Ru_{SA}/ns-Co_3O_4$ was further analyzed, exihibiting two distinct peaks at 1.55 Å and 2.45 Å, attributed to Ru-O and Ru-Ru/Co coordinations, respectively (Fig. 3d). This confirms the synthesis of the Ru-incorporated structure without the formation of Ru nanoclusters or nanoparticles. Intriguingly, the Ru-O peak position in $Ru_{SA}/ns-Co_3O_4$ catalyst, slightly higher than in the pure RuO_2, indicates a manipulated local structure with varied Ru-O bond lengths and lattice distortion in breaking the structural symmetry of the $ns-Co_3O_4$ matrix[35]. Further analysis via EXAFS wavelet transform (WT) discerns radial distance resolution and differentiates backscattering atoms in k-space (Fig. 3e). Notably, two main maxima at 5.0 Å^{-1} and 7.2 Å^{-1} have been shown on $Ru_{SA}/ns-Co_3O_4$, which represent Ru-O and Ru-Co units[35,36], respectively, further indicating the atomic dispersion of Ru atoms in $Ru_{SA}/ns-Co_3O_4$ with the absence of locally aggregated RuO_2 cluster structure. Furthermore, a model-based EXAFS fitting of $Ru_{SA}/ns-Co_3O_4$ indicates that no Ru-Ru scattering can be discovered and the second scattering can be attributed to Ru-Co with a distinct bond distance, which represents Ru-O-Co in the crystal structure (Fig. 3f and Supplementary Fig. 12)[34]. Therefore, we conclusively demonstrate that Ru species exist in the form of single-atom sites with homogeneous dispersion throughout the Co_3O_4 matrix. The photon energy of $Ru_{SA}/ns-Co_3O_4$ shows a negative shift of pre-peak (7709 eV) than Co_3O_4 (Fig. 3g), indicating that the atomic-level Ru doping leads to the local atomic arrangement of Co atoms and the transfer of electrons between $ns-Co_3O_4$ and Ru, as verified by the Co $2p_{3/2}$ XPS results (Supplementary Fig. 13). The corresponding Co K-edge EXAFS of Co_3O_4 and $Ru_{SA}/ns-Co_3O_4$ reveal three distinct peaks, identified as Co-O, octahedral Co-Co (Co_{Oh}-Co_{Oh}) and tetrahedral Co-Co bonds (Co-Co_{Td}), respectively (Fig. 3h)[34,35]. Compared with Co_3O_4, $Ru_{SA}/ns-Co_3O_4$ shows a slightly increased ratio of Co_{Oh}-Co_{Oh} coordination to Co-Co_{Td} coordination. This indicates a slightly increased ratio of octahedron to tetrahedron sites[35]. This evidence further substantiates that the incorporated Ru species preferentially occupies the octahedron site in the spinel Co_3O_4 structure, which enhances its structural stability.

Electrochemical hydrogenation performance measurement

We first assessed the ECH performance in a standard three-electrode H-cell configuration in 1 M KOH with 50 mM quinoxaline. The different Ru

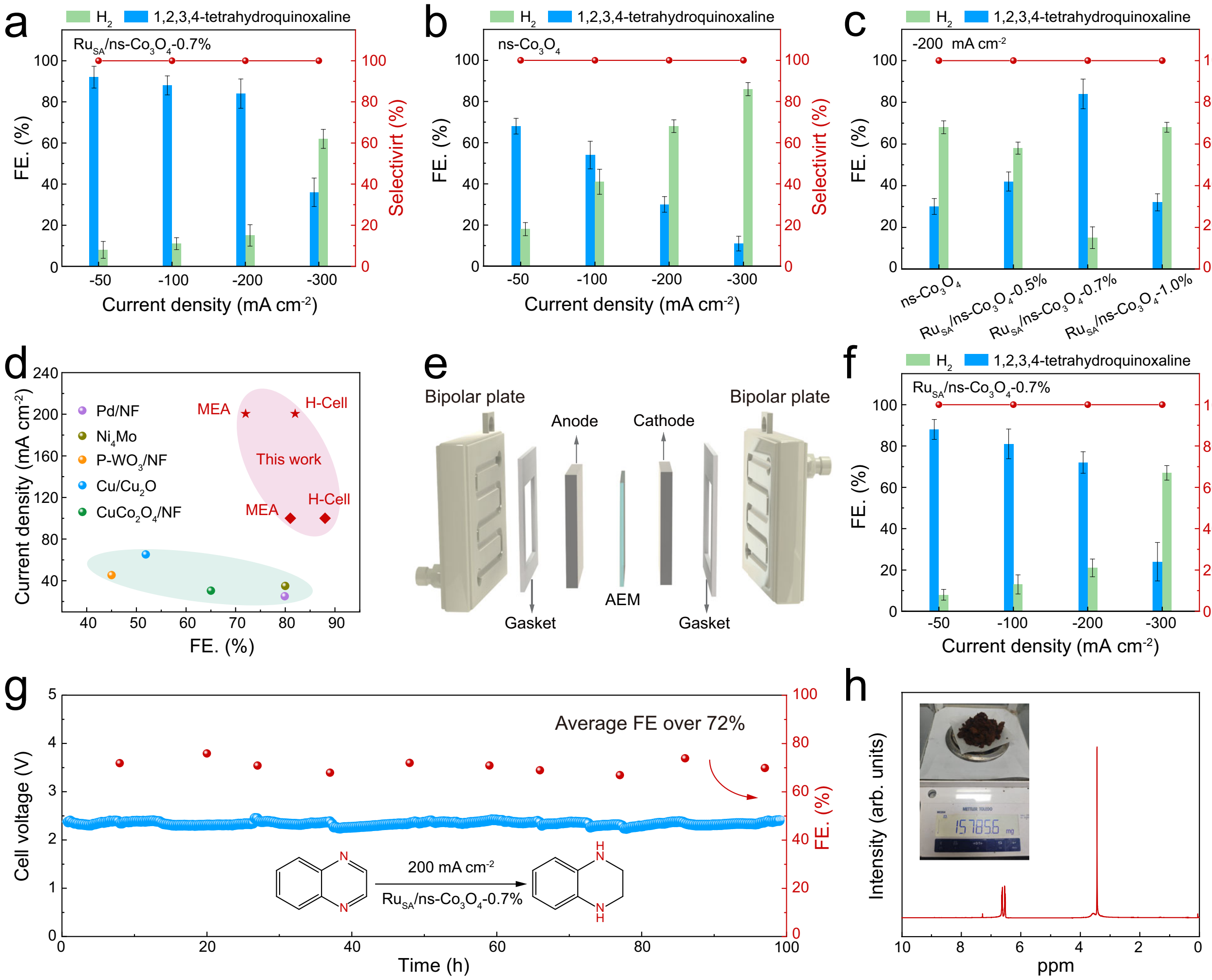

Fig. 4 | Electrochemical hydrogenation performance. a The FE of 1,2,3,4-tetrahydroquinoxaline and H_2 over Ru_{SA}/ns-Co_3O_4-0.7% in 1 M KOH with 50 mM quinoxaline passed 193 C at different current density. **b** The FE of 1,2,3,4-tetrahydroquinoxaline and H_2 over ns-Co_3O_4 in 1 M KOH with 50 mM quinoxaline passed 193 C at different current density. **c** The FE of 1,2,3,4-tetrahydroquinoxaline and H_2 over ns-Co_3O_4, Ru_{SA}/ns-Co_3O_4-0.5%, Ru_{SA}/ns-Co_3O_4-0.7% and Ru_{SA}/ns-Co_3O_4-1.0% in 1 M KOH with 50 mM quinoxaline passed 193 C at 200 mA cm^{-2}. **d** Comparison of the ECH of quinoxaline/quinoline performance with other catalysts reported in the literature. **e** The schematic diagram of MEA system. **f** The FE of 1,2,3,4-tetrahydroquinoxaline and H_2 over Ru_{SA}/ns-Co_3O_4 at different current densities in MEA. **g** Stability evaluation of the Ru_{SA}/ns-Co_3O_4-0.7% at 200 mA cm^{-2}, in which 500 mL of the 1 M KOH aqueous solution containing 50 mM quinoxaline was circularly fed. Cell voltage without iR-correction. **h** 1,2,3,4-Tetrahydroquinoxaline products and the corresponding ^1H NMR result after ECH of quinoxaline using Ru_{SA}/ns-Co_3O_4-0.7% in MEA. Inset: Optical image of the obtained solid product. Error bars in (**a**, **b**, **c**, **f**) represent the standard deviation from three independent measurements. FE Faradaic efficiency; sel selectivity. Source data are provided as a Source Data File.

loadings in the Co_3O_4 nanosheets could be created through tuning the compositions of precursor alloys (Supplementary Figs. 8, 14, 15 and Supplementary Table S1). Linear sweep voltammetry (LSV) curves reveal that the Ru SAs catalyst exhibits significantly higher current density than ns-Co_3O_4, indicating that Ru single atoms can promote the hydrogenation activity and kinetics of quinoxaline (Supplementary Fig. 16). In particular, it is found that the catalytic activities and FE of Ru SAs catalysts are superior to ns-Co_3O_4, illustrating that the introduction of Ru single atoms is more favourable for ECH of quinoxaline, especially at large current densities (Fig. 4a, b and Supplementary Figs. 17–19). Specifically, Ru_{SA}/ns-Co_3O_4-0.7% presents a high FE of 82% at 200 mA cm^{-2}, which is higher than those of Ru_{SA}/ns-Co_3O_4-0.5% (~42%) and Ru_{SA}/ns-Co_3O_4-1.0% (~32%) (Fig. 4c). Notably, a nearly 100% carbon balance was achieved, verifying the exclusive conversion of quinoxaline to the target product 1,2,3,4-tetrahydroquinoxaline (Supplementary Figs. 20). Such a high FE and large current density over Ru_{SA}/ns-Co_3O_4-0.7% still have high levels relative to other reported state-of-the-art electrocatalysts (Fig. 4d and Supplementary Table 1)[9–12,37]. These results indicate that the Ru_{SA}/ns-Co_3O_4-0.7% could enhance quinoxaline hydrogenation activity at industrial-level current densities, primarily attributed to the dynamic equilibrium between active hydrogen generation and consumption established on the catalyst surface. Significantly, the Ru_{SA}/ns-Co_3O_4 exhibits high electrochemical hydrogenation performance toward other N-heterocyclic compounds, achieving a conversion rate of >90% and a selectivity of ~100% (Supplementary Figs. 21–27), which is significantly superior to that of ns-Co_3O_4, thus validating the generality of the proposed strategy.

To further validate the potential of Ru_{SA}/ns-Co_3O_4 in practical applications, the electrochemical activity and stability of Ru_{SA}/ns-Co_3O_4-0.7% were investigated with MEA electrolyser at different industrial-level current densities (Fig. 4e, f). In comparison with the high cell voltage of water splitting without the addition of quinoxaline, the cell voltages are significantly decreased after adding quinoxaline, indicating that the ECH of quinoxaline process is kinetically more favorable (Supplementary Fig. 28). Notably, Ru_{SA}/ns-Co_3O_4-0.7% maintained the high FE of 1,2,3,4-tetrahydroquinoxaline at 200 mA cm^{-2} for 100 h under continuous electrolysis (Fig. 4g). Importantly, 15.7 g of 1,2,3,4-tetrahydroquinoxaline as the

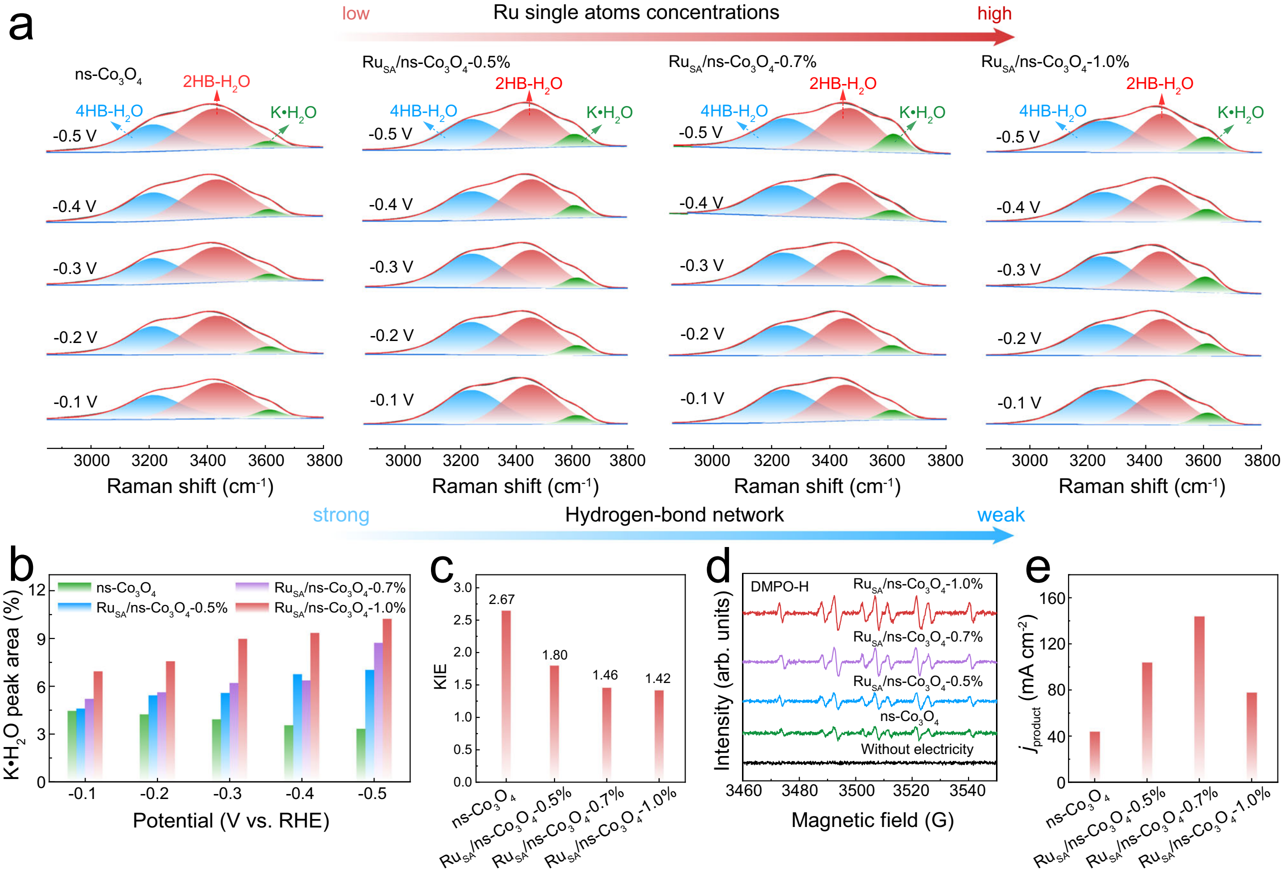

Fig. 5 | Microenvironment study from in situ characterizations. **a** Potential-dependent in situ Raman spectra of the O-H stretching mode of interfacial water on ns-Co_3O_4 with different Ru SA loading without iR correction. **b** Estimated proportions of K•H_2O from the peak areas on ns-Co_3O_4 with different Ru SA loading. **c** Calculated KIE values (J_{H_2O}/J_{D_2O}) on the ns-Co_3O_4 with different Ru SA loadings at −0.3 V vs. RHE without iR correction. **d** Quasi-in situ EPR spectra detected from the electrochemical reactions on the ns-Co_3O_4 with different Ru SA loadings in 1 M KOH at −0.1 V vs. RHE using DMPO as the spin-trapping agent without iR correction. **e** A volcano-like relationship between Ru single atoms concentrations and partial current densities of 1,2,3,4-tetrahydroquinoxaline on these catalysts at −200 mA cm^{-2}. Source data are provided as a Source Data File.

hydrogenated product is obtained (Fig. 4h), further highlighting the high potential for industrial-level ECH of quinoxaline to 1,2,3,4-tetrahydroquinoxaline. Meanwhile, the morphology and compositions of Ru_{SA}/ns-Co_3O_4-0.7% can well retained without obvious damage after the long-term stability test (Supplementary Figs. 29–32), which confirms their ability to maintain high current density and FE due to the structural stability.

In addition, we conducted a preliminary technoeconomic analysis (TEA) using a model adapted in the literature[38,39], which includes the costs of capital, maintenance, installation, input chemicals, and operation, to investigate the feasibility of this coupling system (Supplementary Fig. 33, Supplementary Note 1 and Supplementary Table 3). The cost and revenue of the ECH||OER system were calculated to be ~$400.3136/ton quinoxaline and ~$1033/ton 1,2,3,4-tetrahydroquinoxaline, respectively, thus the profit was calculated to be $632.6864/ton 1,2,3,4-tetrahydroquinoxaline (Supplementary Fig. 34).

In situ investigations for interface water

Given that H* only originates from interfacial water in alkaline environments, regulating interfacial water behavior is crucial for promoting HO-H bond dissociation and providing sufficient H*[40]. In situ Raman spectroscopy was firstly performed to reveal the precise mechanism of interfacial water manipulation by Ru SAs. The broad O-H stretching peak of interfacial water can be Gaussian fitted into three distinct components, Raman peaks located at ~3200, ~3400, and ~3600 cm^{-1} are attributed to 4-coordinated hydrogen-bonded water (4HB-H_2O), 2-coordinated hydrogen-bonded water (2HB-H_2O), and free water (K•H_2O), among which the K•H_2O with the weakest hydrogen-bond interaction requires the lowest activation energy to break the covalent O−H bond of H_2O (Fig. 5a)[41–43]. Compared with that of ns-Co_3O_4, the larger proportion of K•H_2O on Ru_{SA}/ns-Co_3O_4 at different potentials indicates weaken hydrogen-bond networks at the electrode–electrolyte interface (Fig. 5a and Supplementary Fig. 35). Besides, with the potential decreases, the proportion of K•H_2O on Ru_{SA}/ns-Co_3O_4 slightly increased, whereas it is depleted on ns-Co_3O_4 (Fig. 5b). This different behavior is attributed to Ru SAs induced asymmetric local electric field, which could beneficial for the reconfiguration of interfacial water and disrupt the connectivity of hydrogen-bond network in the electric double layer. Because of the lack of constraint of hydrogen bonds, K•H_2O is more inclined to transform into the H-down structure at negative potentials than 2HB-H_2O and 4HB-H_2O (Supplementary Fig. 36)[30], thereby leading to facilitated dynamic evolution from hydrogen bond water to K•H_2O, and constructing continuous K•H_2O enriched environment. For these catalysts, 4HB-H_2O remains the predominant species across all detected potentials, ensuring efficient proton transfer during the water dissociation process (Supplementary Fig. 37). In contrast, the 2-HB•H_2O species decreases gradually with increasing Ru single atom concentration, indicating that 2-HB•H_2O gradually transforms into K•H_2O (Supplementary Fig. 38)[44]. Additionally, the vibrational frequencies of the adsorbates vary with electrode potentials, which are attributed to the vibrational Stark effect[45]. A steeper Stark slope indicates that

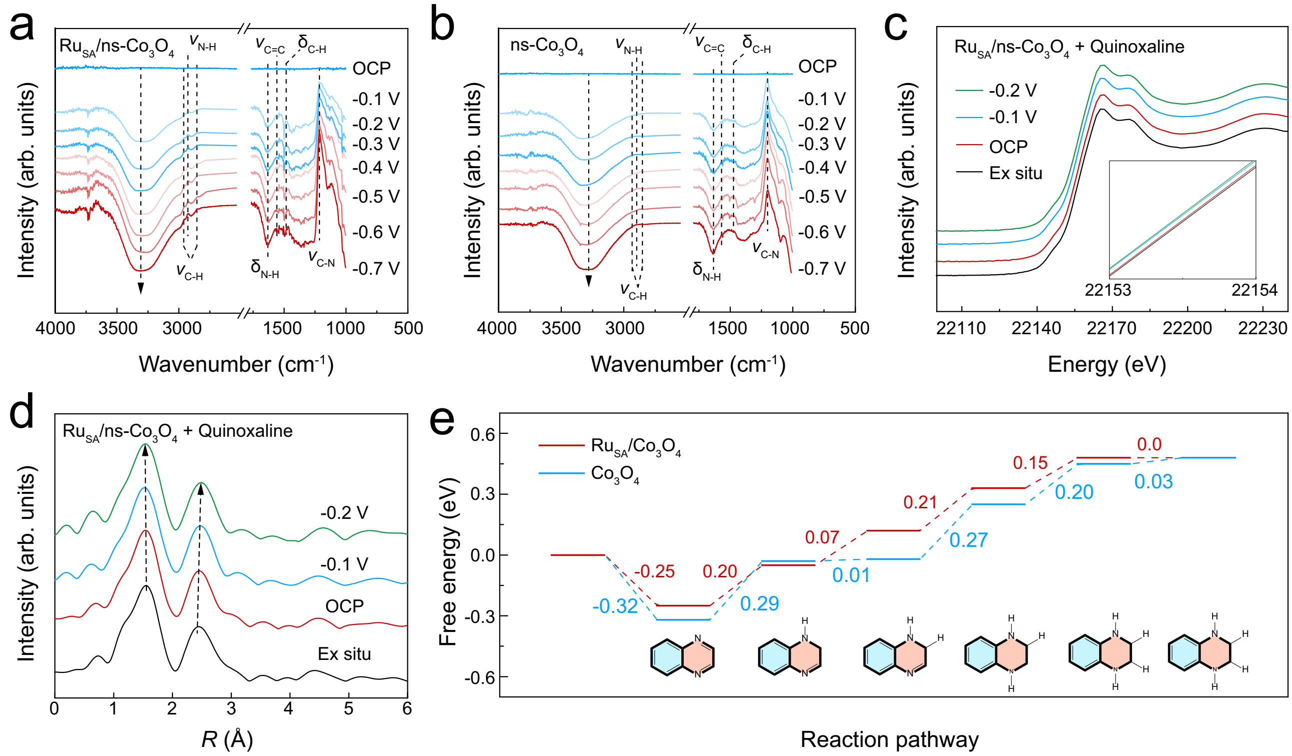

Fig. 6 | Mechanistic study for ECH of quinoxaline. **a**, **b** In situ ATR-SEIRAS measurements under various potentials (V vs. RHE) without iR correction for Ru$_{SA}$/ns-Co$_3$O$_4$ and ns-Co$_3$O$_4$ during ECH of quinoxaline. **c** In situ Ru K-edge XANES spectra of Ru$_{SA}$/ns-Co$_3$O$_4$ recorded in 1 M KOH with quinoxaline under various potentials (V vs. RHE) without iR correction. **d** The corresponding Ru K-edge FT-EXAFS spectra for Ru$_{SA}$/ns-Co$_3$O$_4$. **e** The free-energy diagram for electrochemical hydrogenation of quinoxaline to 1,2,3,4-tetrahydroquinoxaline on Ru$_{SA}$/Co$_3$O$_4$ and Co$_3$O$_4$ through 1,2,3,5,6-H* addition pathways. Source data are provided as a Source Data File.

K•H_2O is more sensitive to the electric field at the cathodic potentials than 4HB-H_2O and 2HB-H_2O (Supplementary Fig. 39)[46]. Kinetic isotopic effect (KIE) tests were further conducted to validate the contribution of asymmetric local electric field to the enhanced H_2O dissociation. The KIE values were calculated by comparing the current density measured in H_2O and D_2O, revealing the proton transfer kinetics during the H_2O splitting process[47]. As a result, the Ru$_{SA}$/ns-Co$_3$O$_4$ shows the much lower KIE value than the ns-Co$_3$O$_4$, indicating that asymmetric local electric field can accelerate the H_2O dissociation process and ensure the H* supply (Fig. 5c, Supplementary Fig. 40). In addition, the electron paramagnetic resonance (EPR) spectrum from Ru$_{SA}$/ns-Co$_3$O$_4$ exhibited a stronger signal than that in ns-Co$_3$O$_4$ at the same applied potential, indicating a higher capability for H* generation on the Ru$_{SA}$/ns-Co$_3$O$_4$, which in line with the KIE results (Fig. 5d)[48]. Taking the sequence of Ru single atom concentrations, we have determined here in combination with the above in situ Raman results and electrochemical performance to accurately establish the relationship between the performance and the structure of H-bond networks, achieving precise control over the activity of ECH. Under high current densities, increasing single-atom concentrations induces the weakening of hydrogen-bond networks with large K•H_2O ratios, accompanied by an increase in the competing HER. Conversely, decreasing single-atom concentrations induces insufficient H* supply and suppresses the kinetics of quinoxaline hydrogenation. This can be further verified in Fig. 5e, where the partial current density of 1,2,3,4-tetrahydroquinoxaline shows a volcano-shaped dependence on the Ru single atom concentrations of these catalysts. The Ru$_{SA}$/ns-Co$_3$O$_4$-0.7% with optimal single atom concentrations reaches the summit of the volcano, which stands out for having excellent industrial-level current densities and durability due to the balance of hydrogen transfer from the reaction microenvironment by tuning the K•H_2O ratios at the electrode–electrolyte interface.

Mechanism investigations for quinoxaline hydrogenation

To investigate the origins of the marked quinoline hydrogenation performance of Ru$_{SA}$/ns-Co$_3$O$_4$ catalyst, we performed in-situ attenuated total reflection surface enhanced infrared absorption (ATR-SEIRAS) spectroscopy to monitor quinoline hydrogenation intermediates under the different potentials (Fig. 6a, b). As the ECH of quinoxaline reaction progresses, the C–N stretching vibration at 1208 cm^{-1} and the C = C backbone vibration at 1560 cm^{-1} show upward band bends, attributing to the N adsorption of quinoxaline and the hydrogenation of the pyrazine ring, respectively. The vibration peaks of $-CH_2-$ at 1496, 2853, and 2960 cm^{-1} bend downward, which indicates the hydrogenation of the pyrazine ring of quinoxaline. In addition, the generation of *$C_8H_7N_2$ radical intermediate was also observed by the downward bend of the stretching vibration of N–H at 2929 cm^{-1} and the bending vibration of N–H at 1631 cm^{-1}. The changes observed in the N–H, $-CH_2-$, C=C, C–N, and O–H signals demonstrate the effective adsorption and hydrogenation process of quinoxaline on catalyst sites[49]. However, compared with ns-Co$_3$O$_4$, Ru$_{SA}$/ns-Co$_3$O$_4$ exhibits a notably strong adsorption reaction generation peak, which is attributed to the more vigorous H_2O dissociation on Ru$_{SA}$/ns-Co$_3$O$_4$ to generate more H* for the ECH of quinoxaline to increase product formation, which is further confirmed by the H* scavenging experiment with tert-butylalcohol (TBA) (Supplementary Fig. 41). In situ X-ray absorption spectroscopy (XAS) measurements were further conducted to analyze the catalytic behavior of Ru$_{SA}$/ns-Co$_3$O$_4$ in 1 M KOH with quinoxaline. As the applied potential was decreased from the open circuit potential (OCP) to −0.2 V vs. RHE, the absorption edge of the Ru K-edge XANES spectra progressively shifted toward lower energies, indicating a decrease in the oxidation state of Ru (Fig. 6c). Moreover, compared to the OCP, the first coordination shell structure of the Ru-O bond showed no significant changes at potentials of −0.1 V and −0.2 V vs. RHE, indicating that quinoxaline molecules did not adsorb on the Ru sites. Notably, the FT-EXAFS spectra show a slight shift in the peak position of the second coordination shell associated with the Ru-Co bond under applied potentials. These shifts imply that the H_2O dissociation and quinoxaline hydrogenation at Co sites alter the local electronic structure and atomic configuration, and indirectly modulate the FT-EXAFS signal of Ru through electronic coupling and structural communication via the Ru-Co bond (Fig. 6d). Therefore, these results indicate that Co sites serve as the main active sites for the ECH of quinoxaline. The in situ experimental results demonstrate that the Ru SAs primarily enhanced H_2O dissociation dynamics while generating sufficient H*, thereby effectively driving the ECH of quinoxaline to 1,2,3,4-tetrahydroquinoxaline on the Co_3O_4 matrix.

The hydrogenation reaction mechanism of quinoxaline was further investigated through DFT calculations. The 1,2,3,5,6- and 1,2,4,5,6-H* addition pathways are two possible pathways for electrochemical hydrogenation of quinoxaline in water (Supplementary Fig. 42). According to theoretical calculations, the 1,2,3,5,6-H* addition pathway is more favorable (Supplementary Figs. 43–47). Free energies for the distinct hydrogenation sequences on the two catalysts were calculated (Fig. 6e). Upon analyzing the reaction free energies of the pathway, it is observed that the first hydrogenation of quinoxaline exhibits reaction barriers of 0.29 and 0.20 eV for the Co_3O_4 and Ru_{SA}/Co_3O_4, respectively. Notably, the highest activation barrier of this first hydrogenation step serves as the rate-determining step for both catalysts. However, in the second hydrogenation step, there is a significant disparity in the activation energies between these two catalysts. Co_3O_4 exhibits a substantially lower reaction barrier of 0.01 eV compared to Ru_{SA}/Co_3O_4 (0.07 eV). Nevertheless, for the subsequent steps of hydrogenation, the energy barrier of Ru_{SA}/Co_3O_4 is significantly lower than that of Co_3O_4, offering a much faster kinetics for the hydrogenation. Besides, H* is preferentially hydrogenated for quinoxaline rather than undergoing self-coupling to release H_2, which accounts for the high FE of the ECH process (Supplementary Figs. 48–51). Therefore, Ru SAs can optimize the hydrogenation step and improve the hydrogenation reaction activity of quinoxaline, as experimentally confirmed by the quasi-in situ EPR results (Supplementary Fig 52).

Discussion

In summary, we have demonstrated a series of Ru SAs doped Co_3O_4 nanosheet catalysts, which could precisely modulate the reorientation of K•H_2O by tuning their Ru single atom concentrations to achieve industrial-level electrochemical hydrogenation of quinoxaline to 1,2,3,4-tetrahydroquinoxaline. The results of both AIMD simulations and DFT calculations indicate that the asymmetric local electric field can induce strong hydrogen-bonded interactions between Ru_{SA}/Co_3O_4 and interfacial H_2O, which can boost H_2O dissociation with adequate H* supply, and the spontaneous hydrogen transfer can accelerate hydrogenation of quinoxaline to 1,2,3,4-tetrahydroquinoxaline. In situ spectroscopic characterizations reveal the crucial role of Ru single-atom concentrations in regulating the interfacial H_2O structures for facilitating the electrochemical hydrogenation reactions, which also accurately established the relationship between the performance and the structure of H-bond networks, achieving precise control over the activity of ECH. The MEA electrolyser assembled by utilizing Ru_{SA}/ns-Co_3O_4-0.7% as cathode can steadily operate at 200 mA cm^{-2} with an average FE of 72% for 100 h. This work not only achieved efficient electrochemical hydrogenation of quinoxaline under industrial-level current densities but also established a valuable framework for applying interfacial water regulation in electrochemical hydrogenation reactions.

Methods

Materials

Aluminum foil (99.999%), Ruthenium foil (99.99%) and Cobalt foil (99.99%) were purchased from Beijing Jiaming Platinum Nonferrous Metals Co., Ltd. Quinoxaline (98%), Isoquinoline (97%), Pyridine (99.5%), Quinoline (99%), and Tert-butylalcohol (99.5%) were purchased from Adamas. Ethyl Acetate (99.7%) and KOH (95%) were purchased from Greagent. All chemicals were used without further purification.

Preparation of Ru_{SA}/Co_3O_4 nanosheet alloy. $Al_{80}Co_{20\text{-}x}Ru_x$ ($x = 0$, 0.1, 0.2, 0.3) ribbons were prepared via a melt-spinning process. The precursor ribbons were then prepared via a two-step method. Firstly, 200 mg of $Al_{80}Co_{20\text{-}x}Ru_x$ ribbons was put into 200 mL of 2 M KOH aqueous solution to remove Al in the ribbons. The etching reaction was at room temperature for around 10 h until no apparent bubbles were observed and obtained Ru/ns-CoO_x. The as-prepared product was washed with ultra-pure water and alcohol several times. After the washing process, the product was dried in a vacuum oven at 60 °C for 24 h. The second-step calcination was carried out in air at 300 °C for 3 h.

Characterizations. XRD patterns of the samples were conducted by using a Bruker D8 Advance X-ray diffractometer with Cu Kαradiation ($\lambda = 1.5418$ Å). Morphology and chemical composition were collected via MIR3 TESCAN SEM equipped with an Oxford energy dispersive X-ray spectroscope. HAADF-STEM and EDS mapping were conducted on a JEM-ARM 200 F with double spherical aberration (Cs) correctors for both the probe forming and image-forming objective lenses at an accelerating voltage of 200 kV. The chemical state and composition of the samples were characterized using XPS (Thermo Scientific Escalab 250Xi) with an Al Kα monochromatic (150 W, 20 eV pass energy, 500 μm spot size). NMR spectra were obtained on a Bruker Avance III HD 400-MHz spectrometer with $CDCl_3$ as the solvent. EPR spectra were recorded with a Bruker EMX plus-6/1 spectrometer.

In situ XAS electrochemical measurements. The XAS experiments were carried out at BL11B at Shanghai Synchrotron Radiation Facility. A home-made Teflon electrochemical cell with an electrochemical workstation (Ivium, Compact Stat.) was employed for in situ XAS measurement under the sensitive fluorescence model (Supplementary Fig. 53). With adding quinoxaline to a cell filled with 1.0 M KOH electrolyte. A graphite rod was used as the counter electrode, and a Hg/HgO electrode was used as the reference electrode. The carbon paper loaded with catalyst as the working electrode was in contact with Kapton tape to the observation window of the cell. During the experimental measurement, different potentials of OCP, −0.1 and −0.2 V vs. RHE were applied to the system, and each potential was maintained to collect spectra for 10 min. The acquired XAS data were processed using Athena software. All the voltages indicated in the "Methods" section has not been iR corrected.

In situ ATR-SEIRAS measurements. Electrochemical in situ ATR-SEIRAS measurements were performed in internal reflection mode on a Thermo Fisher Nicolet iS50 (equipped with an ElectroChemIR unit from Pike Technologies). The experiments were carried out in a three-electrode system: The catalyst ink was dripped onto a monocrystalline silicon covered with an Au membrane, which served as the working electrode, Hg/HgO is introduced as a reference electrode near the working electrode, and a Pt wire is used as the counter electrode. We first reduced the catalyst in 1 M KOH for 10 min at −0.1 V vs. RHE, then 50 mM quinoxaline was added in the electrolyte for in situ ATR-SEIRAS test. The potential range was from OCP to −0.7 V (vs. RHE), with spectra collected at a spectral resolution of 4 cm^{-1} with at least 32 coadded scans. The CHI 760E electrochemical workstation was used to control the potential during the ATR-SEIRAS test.

In situ Raman measurements. Electrochemical in situ Raman measurements were carried out by Renishaw inVia Qontor Raman microscope. The excitation wavelength of the semiconductor laser was 532 nm. All the Raman measurements were performed with a 50× microscope objective. Raman frequencies were calibrated using silicon wafers before the experiment. A three-electrode Raman cell with an embedded quartz window was used for Raman experiments, with a platinum wire as counter electrode and Hg/HgO electrode as reference electrode. A glassy carbon electrode loaded with a catalyst was used as a working electrode. 1 M KOH solution was used as electrolyte. The CHI 760E electrochemical workstation was used to control the potential during the Raman test.

Electrochemical measurements. The electrochemical measurements were carried out on CHI 760E workstation. All the experiments were carried out at room temperature. All electrolytes used in the tests were freshly prepared and used immediately. Electrochemical measurements were carried out in a divided two-compartment electrochemical cell (Tianjin Aida Hengsheng Technology Development Co., Ltd.) consisting of a working electrode, a carbon rod counter-electrode, and a Hg/HgO reference electrode (Tianjin Aida Hengsheng Technology Development Co., Ltd.). The cathode cell and anode cell containing 10 mL 1.0 M KOH, were separated by an anion exchange membrane (A40-HCO3, 40 μm). 0.5 mmol of quinoxaline was added into the cathode and stirred to form a homogeneous solution. Then, chronoamperometry was carried out at a given constant current and until reaching 193 °C. The liquid products were extracted with ethyl acetate and then quantified by gas chromatography (Shimadzu, GC-2010 Plus) equipped with a flame ionization detector (FID). In a typical procedure of the fabrication of the working electrode, the catalyst ink was prepared by dispersing 5 mg of catalysts into a mixture solution of 0.48 mL ethanol and 20 μL of Nafion solution (5%, w/w, Alfa Aesar) with sonication for 30 min. Fifty microliters of the electrocatalyst ink was loaded onto a carbon paper with an area of $1 \times 1\,\mathrm{cm}^2$ by drop-coating with the loading mass of catalyst is $0.50\,\mathrm{mg\,cm}^{-2}$. The as-prepared catalyst film was dried at room temperature. And ECH of quinoxaline durability measurements at large current densities were measured in a commercial $1 \times 1\,\mathrm{cm}^2$ MEA electrolyzer with a two-electrode system, in which IrO_x/Ti foam served as the anode electrode. The catalysts ($1.5\,\mathrm{mg\,cm}^{-2}$) and Nafion (5%) were ultrasonically mixed and then were drop-coating on anion-exchange membrane (A40-HCO3, 40 μm), which served as the cathode electrode. The anion exchange membrane was soaked in 0.5 M KOH aqueous solution for 2 h and rinsed repeatedly with ultrapure water for pretreatment. And an anion-exchange membrane was located between the cathode and anode to separate chambers. The full-cell potentials in the two-electrode MEA system were shown without iR correction. During ECH of quinoxaline in MEA electrolyzer, the anode electrolyte (1.0 M KOH) and cathode electrolyte (1.0 M KOH + 50 mM quinoxaline) flowed through the anode and cathode at a flow rate of $20\,\mathrm{mL\,min}^{-1}$. All potentials measured were calibrated to RHE using the following equation: $E_{\mathrm{RHE}} = E_{\mathrm{Hg/HgO}} + 0.098 + 0.059 \times \mathrm{pH}$ (pH 13.7 ± 0.3).

Quantitative reductive product. The conversion (%), selectivity (%), and Faradaic efficiency (FE, %) of 1,2,3,4-tetrahydroquinoxaline were calculated using Eqs. (1)–(3):

$$\mathrm{Conversion}(\%) = \frac{\text{mol of formed product}}{\text{mol of initial reactant}} \times 100\% \quad (1)$$

$$\mathrm{Selectivity}(\%) = \frac{\text{mol of formed product}}{\text{mol of consumed reactant}} \times 100\% \quad (2)$$

$$\mathrm{FE}(\%) = \frac{\mathrm{nmF}}{\mathrm{It}} \times 100\% \quad (3)$$

where n = Number of transferred electrons
m = Amount of substance
F = Faradaic's constant
I = Total current
t = Electrolysis time

Scavenge of high active H* with *t*-BuOH. A total of 0.5 mmol of quinoxaline was added into the electrolytic cell with 10 mL KOH for the following hydrogenation with/without*t*-BuOH. Chronoamperometry was carried out at $-100\,\mathrm{mA\,cm}^{-2}$ for 193 °C in 1 M KOH.

Calculate H_2O dissociation. The Co_3O_4 (222) was built by cleaving the Co_3O_4 2 × 2 × 2 supercell, which includes seven atomic layers and carries Co atoms on the top layer. The Ru_{SA}/Co_3O_4 (222) was modeled by replacing one top octahedral Co atom with Ru atom. In the cases of Co_3O_4 (222) and Ru_{SA}/Co_3O_4 (222), one and two reactants were considered, respectively, i.e., H_2O on the top of Co atom for the former and H_2O on the top of Ru atom or Co atom (that is close to Ru atom) for the latter. A ~12 Å vacuum was added along the direction normal to the surface. The search of transition states (TS) for H_2O dissociation was performed by spin-unrestricted density functional theory (DFT) calculations in the CASTEP code[50], before which the reactants and products were optimized with the convergence tolerances of energy, maximum force, and maximum displacement of 2.0×10^{-5} eV/atom, 0.05 eV/Å, and 0.002 Å, respectively. The complete LST/QST was adopted as the search protocol, where the LST (linear synchronous transit) was first performed and then followed by repeated conjugate gradient minimizations and QST (quadratic synchronous transit) maximizations until a TS was located. In these calculations, the generalized gradient approximation (GGA) with the Perdew-Burke-Ernzerhof (PBE) functional was used for the description of the exchange and correlation effects; the Grimme method for the DFT-D correction[51,52]; 500 eV for the energy cutoff; 1 × 1 × 1 k-points meshes for Brillouin zone sampling; and OTFG ultrasoft for the pseudopotential.

Analysis of electron density difference. Based on the optimized Co_3O_4 (222) and Ru_{SA}/Co_3O_4 (222) models, the electron density difference with respect to the sum of the atomic densities was analyzed by using the CASTEP code[50].

Examination of free-energy evolution during the hydrogenation processes. Based on the computational hydrogen electrode (CHE) model, in which the chemical potential of a proton-electron pair is taken by the one-half of the chemical potential of H_2 (g) at standard hydrogen electrode conditions[53,54], the difference of Gibbs free energies between two reaction intermediates were evaluated by:

$$\Delta G_{\mathrm{H}}^{(n+1)\mathrm{H}} = G^{*}_{(n+1)\mathrm{H}} - G^{*}_{n\mathrm{H}} 1/2 G_{\mathrm{H2}} \quad (4)$$

where $G^{*}_{(n+1)H}$, G^{*}_{nH}, and G_{H2} denote the Gibbs free energy of the adsorption system after adding one H, the adsorption system before adding one H, and the H_2 molecule. The spin-unrestricted DFT calculations were carried out in the DMol3 code, where the related adsorption systems and H_2 molecule were first optimized and then their frequencies were calculated and analyzed to obtain the free energies at 298.15 K.

Ab-initio molecular simulations of H_2O molecules

A layer with 24 H_2O molecules was placed on the Co_3O_4 (222) and Ru_{SA}/Co_3O_4 (222) surfaces modeled above, respectively. After adding a vacuum larger than ~12 Å out of the surface, geometry optimizations were first carried out with the convergence tolerances of energy, maximum force, and displacement of 2.0×10^{-5} Ha, 0.004 Ha/Å, and 0.005 Å, respectively. The relevant spin-unrestricted DFT calculations were executed in the DMol3 code and at the GGA PBE level[51,55,56]. The DFT Semi-core Pseudopots (DSPP) was employed for core treatment; a smearing of 0.05 Ha for the orbital occupation; the Grimme method for the DFT-D correction[52]; and 1 × 1 × 1 k-points meshes for Brillouin zone sampling. Then, ab-initio molecular dynamics simulations were performed on the two optimized systems, respectively, with the NVT (constant number of molecules, volume, and temperature) ensemble at a temperature of 298.15 K for 2.5 ps. Here, the time step was set as 1 fs and the Massive GGM thermostat was adopted for temperature control.

Data availability

The data generated in this study are provided in the Supplementary Information/Source Data file. Source data are provided with this paper.

References

1. Kleinhaus, J. T. et al. Developing electrochemical hydrogenation towards industrial application. *Chem. Soc. Rev.* **52**, 7305–7332 (2023).
2. Shu, Y. et al. Fragmented ultrathin carbon buffed copper clusters for selective hydrogenation of N-Heteroarenes under ambient pressure. *J. Am. Chem. Soc.* **147**, 15578–15590 (2025).
3. Dong, C. et al. Fully exposed palladium cluster catalysts enable hydrogen production from nitrogen heterocycles. *Nat. Catal.* **5**, 485–493 (2022).
4. Liu, C., Liu, X. & Liu, Q. Stereodivergent asymmetric hydrogenation of quinoxalines. *Chem* **9**, 2585–2600 (2023).
5. Zhang, M. et al. Consecutive asymmetric transfer hydrogenation of C2-acylated quinolines and quinoxalines: a diastereodivergent synthesis of enantioenriched tetrahydroquinolines and tetrahydroquinoxalines bearing endo- and exocyclic chirality. *J. Am. Chem. Soc.* **147**, 18197–18207 (2025).
6. Teh, W. J. et al. Selective electroreduction of acetylene to 1,3-butadiene on iodide-induced $Cu^{\delta+}$–Cu^0 sites. *Nat. Catal.* **7**, 1382–1393 (2024).
7. Zhao, B.-H. et al. Economically viable electrochemical ethylene production with high yield and selectivity. *Nat. Sustain.* **6**, 827–837 (2023).
8. Lin, J. et al. Efficient electroreduction of carbonyl compounds to alcohols over Fe/Fe_2O_3 interfaces. *Nat. Catal.* **8**, 338–347 (2025).
9. Wang, S. et al. Reversible electrochemical hydrogen storage of quinoxaline utilizing Pd/NF dual-function electrocatalyst under mild conditions. *Int. J. Hydrog. Energ.* **49**, 719–728 (2024).
10. Wang, S. et al. Highly selective interconversion of quinoxaline and 1,2,3,4-tetrahydroquinoxaline over a spinel $CuCo_2O_4$ electrocatalyst supported by Ni foam. *Chem. Phys. Lett.* **856**, 141638 (2024).
11. Li, M., Liu, C. & Zhang, B. Using water as the hydrogen source for electrochemical transfer hydrogen storage. *Sci. Bull.* **66**, 1047–1049 (2021).
12. Wang, S. et al. Efficient electrochemical hydrogenation and dehydrogenation of quinoxaline over a dendritic structure P-WO_3/NF electrode. *Mol. Catal.* **554**, 113842 (2024).
13. Zhou, P. et al. Electrochemical hydrogenation of furfural in aqueous acetic acid media with enhanced 2-methylfuran selectivity using CuPd bimetallic catalysts. *Angew. Chem. Int. Ed.* **61**, e202117809 (2022).
14. Shao, J. et al. Electrochemical synthesis of ammonia from nitric oxide using a copper–tin alloy catalyst. *Nat. Energy* **8**, 1273–1283 (2023).
15. Zhu, K. et al. Unraveling the role of interfacial water structure in electrochemical semihydrogenation of alkynes. *ACS Catal.* **12**, 4840–4847 (2022).
16. Shen, H. et al. Durable anion exchange membrane water electrolysis in low-alkaline concentration electrolyte. *J. Am. Chem. Soc.* **147**, 22677–22685 (2025).
17. Mao, J. et al. Electrochemical lithiation regulates the active hydrogen supply on Ru–Sn nanowires for hydrogen evolution toward the high-performing anion exchange membrane water electrolyzer. *J. Am. Chem. Soc.* **147**, 7711–7720 (2025).
18. Li, P. et al. Kinetic cation effect in alkaline hydrogen electrocatalysis and double layer proton transfer. *Nat. Commun.* **16**, 1844 (2025).
19. Deng, L. et al. Lewis Acid-mediated interfacial water supply for sustainable proton exchange membrane water electrolysis. *J. Am. Chem. Soc.* **146**, 35438–35448 (2024).
20. Yang, C. et al. Bioinspired Sulfo oxygen bridges optimize interfacial water structure for enhanced hydrogen oxidation and evolution reactions. *Nat. Commun.* **16**, 6459 (2025).
21. Jiang, K. et al. Manipulating interfacial water via metallic Pt_1Co_6 sites on self-adaptive metal phosphides to enhance water electrolysis. *Adv. Mater.* **37**, 2419644 (2025).
22. Zhao, R. et al. Pd single atoms guided proton transfer along an interfacial hydrogen bond network for efficient electrochemical hydrogenation. *Sci. Adv.* **11**, eadu1602 (2025).
23. Geng, H.-F. et al. The critical role of local microenvironments. *Nat. Catal.* **8**, 753–754 (2025).
24. Meng, L. et al. Alloying and confinement effects on hierarchically nanoporous CuAu for efficient electrochemical semi-hydrogenation of terminal alkynes. *Nat. Commun.* **15**, 5999 (2024).
25. Zhang, H., Raciti, D. & Hall, A. S. Disordered interfacial H_2O promotes electrochemical C–C coupling. *Nat. Chem.* **17**, 1161–1168 (2025).
26. Ji, K. et al. Steering selectivity in electrocatalytic furfural reduction via electrode–electrolyte interface modification. *J. Am. Chem. Soc.* **146**, 11876–11886 (2024).
27. He, M. et al. Microenvironment regulation breaks the Faradaic efficiency-current density trade-off for electrochemical deuteration using D_2O. *Nat. Commun.* **15**, 5231 (2024).
28. Zhang, W. et al. Surfactant directionally assembled at the electrode-electrolyte interface for facilitating electrocatalytic aldehyde hydrogenation. *Angew. Chem. Int. Ed.* **63**, e202407121 (2024).
29. Zhao, Y. et al. A cosolvent electrolyte boosting electrochemical alkynol semihydrogenation. *J. Am. Chem. Soc.* **147**, 1938–1947 (2025).
30. Cai, C. et al. Atomically local electric field induced interface water reorientation for alkaline hydrogen evolution reaction. *Angew. Chem. Int. Ed.* **62**, e202300873 (2023).
31. Li, C.-Y. et al. In situ probing electrified interfacial water structures at atomically flat surfaces. *Nat. Mater.* **18**, 697–701 (2019).
32. Li, Y. et al. A perspective review on N-heterocycles as liquid organic hydrogen carriers and their hydrogenation/dehydrogenation catalysts. *Energy Fuels* **38**, 12447–12471 (2024).
33. Lu, Y. et al. Tuning the selective adsorption site of biomass on Co_3O_4 by Ir single atoms for electrosynthesis. *Adv. Mater.* **33**, 2007056 (2021).
34. Zhu, Y. et al. Iridium single atoms incorporated in Co_3O_4 efficiently catalyze the oxygen evolution in acidic conditions. *Nat. Commun.* **13**, 7754 (2022).
35. Zuo, S. et al. Local compressive strain-induced anti-corrosion over isolated Ru-decorated Co_3O_4 for efficient acidic oxygen evolution. *Nat. Commun.* **15**, 9514 (2024).
36. Li, D. et al. Isolated octahedral Pt-induced electron transfer to ultralow-content ruthenium-doped spinel Co_3O_4 for enhanced acidic overall water splitting. *J. Am. Chem. Soc.* **146**, 28728–28738 (2024).

37. Pan, Y. et al. Electrochemical hydrogenation of quinoline enabled by Cu^0-Cu^+ dual sites coupled with efficient biomass valorization in aqueous solution. *Adv. Funct. Mater.* **35**, 2414120 (2024).
38. Zhou, H. et al. Electrocatalytic upcycling of polyethylene terephthalate to commodity chemicals and H_2 fuel. *Nat. Commun.* **12**, 4679 (2021).
39. Leow, W. et al. Chloride-mediated selective electrosynthesis of ethylene and propylene oxides at high current density. *Science* **368**, 1228–1233 (2020).
40. Zhang, L.-H. et al. Volcano-shaped relationship between interfacial K^+-H_2O ratio and CO_2 reduction activity in tandem electrocatalysts. *Angew. Chem. Int. Ed.* **64**, e202514557 (2025).
41. Wan, Y. et al. Interfacial water regulation for nitrate electroreduction to ammonia at ultralow overpotentials. *Adv. Mater.* **37**, 2417696 (2025).
42. Zhang, S.-N. et al. Ampere-level reduction of pure nitrate by electron-deficient Ru with K^+ ions repelling effect. *Nat. Commun.* **15**, 10877 (2024).
43. Wang, Y.-H. et al. In situ Raman spectroscopy reveals the structure and dissociation of interfacial water. *Nature* **600**, 81–85 (2021).
44. Li, M. et al. Manipulating interfacial water configuration via constructing asymmetric structure unit for hydrogen production in alkaline seawater. *Adv. Funct. Mater.* e14517 https://doi.org/10.1002/adfm.202514517 (2025).
45. Wang, Y. et al. Interfacial water structure modulation on unconventional phase non-precious metal alloy nanostructures for efficient nitrate electroreduction to ammonia in neutral media. *Angew. Chem. Int. Ed.* **64**, e202508617 (2025).
46. Zou, C. J. et al. Interfacial water on Ag/Ag_2S nanowires enhancing the ethanol selectivity for CO_2 electroreduction. *Adv. Mater.* **37**, 2409575 (2025).
47. Shao, W. et al. Bioinspired proton pump on ferroelectric HfO_2-coupled Ir catalysts with bidirectional hydrogen spillover for pH-universal and superior hydrogen production. *J. Am. Chem. Soc.* **146**, 27486–27498 (2024).
48. Cao, X. et al. Cluster-level heterostructure of PMo_{12}/Cu for efficient and selective electrocatalytic hydrogenation of high-concentration 5-Hydroxymethylfurfural. *J. Am. Chem. Soc.* **146**, 25125–25136 (2024).
49. Du, H. et al. Identifying highly active and selective cobalt X-ides for electrochemical hydrogenation of quinoline. *Adv. Mater.* **36**, 2411090 (2024).
50. Clark, S. J. et al. First principles methods using CASTEP. *Z. Krist.* **220**, 567–570 (2025).
51. Perdew, J. P., Burke, K. & Ernzerhof, M. Generalized gradient approximation made simple. *Phys. Rev. Lett.* **77**, 3865 (1996).
52. Grimme, S. et al. A consistent and accurate ab initio parametrization of density functional dispersion correction (DFT-D) for the 94 elements H-Pu. *J. Chem. Phys.* **132**, 154104 (2010).
53. Nørskov, J. K. et al. Origin of the overpotential for oxygen reduction at a fuel-cell cathode. *J. Phys. Chem. B* **108**, 17886–17892 (2004).
54. Skulason, E. et al. A theoretical evaluation of possible transition metal electro-catalysts for N_2 reduction. *Phys. Chem. Chem. Phys.* **14**, 1235–1245 (2012).
55. Delley, B. An all-electron numerical method for solving the local density functional for polyatomic molecules. *J. Chem. Phys.* **92**, 508 (1990).
56. Delley, B. From molecules to solids with the DMol3 approach. *J. Chem. Phys.* **113**, 7756 (2000).

Acknowledgements

This work was supported by the National Natural Science Foundation of China (no. 52371221 and U23A20554 to Y.W.T.) and Independent Research Project of State Key Laboratory of Advanced Design and Manufacturing Technology for Vehicle Body (no. 72365004 to Y.W.T.). The Raman and STEM tests were performed at the Analytical Instrumentation Center of Hunan University. In situ XAS tests were performed at Shanghai Synchrotron Radiation Facility (SSRF).

Author contributions

Y.W.T. conceived and directed the project. L.H.M. carried out key experiments. T.Y.D., T.H.W., and Q.J. performed theoretical calculations. J.L.L. contributed to the XAS measurements and analyses of the XAS experiment results. C.J.D., F.Y.W., and M.P. contributed to the data analysis. Y.W.T. and L.H.M. wrote the manuscript with input from all other authors. All authors discussed the results and commented on the manuscript.

Competing interests

The authors declare no competing interests.

Additional information

Supplementary information The online version contains supplementary material available at https://doi.org/10.1038/s41467-026-68740-6.

Correspondence and requests for materials should be addressed to Tong-hui Wang or Yongwen Tan.

Peer review information *Nature Communications* thanks Xiao Chen, Kai Liu, Lingxia Zheng and the other anonymous reviewer(s) for their contribution to the peer review of this work. A peer review file is available.